Journal of Materials Chemistry C

ROYAL SOCIETY OF CHEMISTRY

PAPER

View Article Online
View Journal

Cite this: DOI: 10.1039/d6tc00601a

Cost-efficient quinoxaline-based semiconducting polymers: systematic structure–property–morphology correlation toward reliable organic field-effect transistors

Yuta Otake, [a] Atsushi Isobe,[a] Ting-Yu Wang,[b] Chu-Chen Chueh, [b] Masayuki Wakioka [c] and Tsuyoshi Michinobu *[a]

Achieving low-cost, organic semiconducting polymers remains a key challenge for the practical application of organic field-effect transistors (OFETs). To overcome this issue, quinoxaline has attracted considerable attention due to its unique structural advantages and synthetic feasibility. In this study, a series of quinoxaline-based semiconducting polymers were successfully synthesized through systematic tuning of π-linkers and alkyl side chains, with comprehensive evaluation of their OFET performance. Density functional theory calculations revealed that these polymers exhibit highly planar backbone structures stabilized by intramolecular noncovalent interactions. Among the synthesized polymers, a thiophene-linker-incorporated polymer with a short alkyl chain exhibited a hole mobility of 2.45 × 10^{-2} cm^2 V^{-1} s^{-1}, representing an improvement of nearly one order of magnitude over that of conventional PTQ10-based OFETs. Furthermore, the introduction of a fluorinated bithiophene unit as the π-type linker enabled ambipolar charge transport. Grazing-incidence wide-angle X-ray scattering (GIWAXS) results further revealed that all polymers exhibited edge-on orientations conducive to efficient charge transport in OFETs. Collectively, this study provides insights into structure–property–morphology relationships in quinoxaline-based polymers with low synthetic complexity, providing rational molecular design guidelines for scalable semiconducting polymer materials.

Received 25th February 2026,
Accepted 23rd April 2026

DOI: 10.1039/d6tc00601a

rsc.li/materials-c

1. Introduction

Organic field-effect transistors (OFETs) and organic photovoltaic cells (OPVs) have attracted considerable attention as core technologies for next-generation flexible electronics due to their lightweight properties, mechanical flexibility, and compatibility with large-area printing processes.[1–4] Compared to small-molecule materials, semiconducting polymers exhibit superior film-forming capabilities, thermal stability, and mechanical strength, enabling simplified device fabrication through solution processing.[5] Recent rapid breakthroughs in OFET and OPV performance have been achieved through the development of precisely designed donor–acceptor (D–A) copolymers.[6–8] In OPVs, power conversion efficiencies (PCEs) have reached 20%. Meanwhile, in OFETs, charge carrier mobilities in numerous systems have now surpassed 1 cm^2 V^{-1} s^{-1}, rivaling those of inorganic materials.[5,9–11]

Effective strategies for achieving high-performance semiconducting polymers involve enhancing the planarity and rigidity of the conjugated backbone while extending the π-conjugation to strengthen interchain interactions.[12–14] As a result, many high-performance polymers reported in recent years have relied on complex fused-ring skeletons composed of multiple aromatic units.[15] However, synthesizing such fused frameworks typically requires multistep organic reactions and cumbersome purification processes, resulting in high synthesis costs. For example, the synthesis of representative OPV donor materials, D18 and PM6, involves over 15 reaction steps, with reported material costs exceeding \$200 g^{-1} (Fig. 1a).[16] Similarly, high charge carrier mobilities in OFETs were achieved through multi-step synthesis of complex fused aromatic cores, exemplified by materials such as naphthalene diimide (NDI),[17–19] indacenodithiophene (IDT),[20,21] diketopyrrolopyrrole (DPP),[7,22,23] and bithiophene imide (BTI) (Fig. 1b).[24] In addition, the extensive use of organic solvents and generation of substantial chemical waste during multi-step synthesis contribute to environmental pollution.[25–27]

[a] Department of Materials Science and Engineering, Institute of Science Tokyo, 2-12-1 Ookayama, Meguro-ku, Tokyo, 152-8552, Japan. E-mail: michinobu@mct.isct.ac.jp
[b] Department of Chemical Engineering, National Taiwan University, Taipei, 10617, Taiwan
[c] Sagami Chemical Research Institute, 2743-1 Hayakawa, Ayase, Kanagawa, 252-1193, Japan

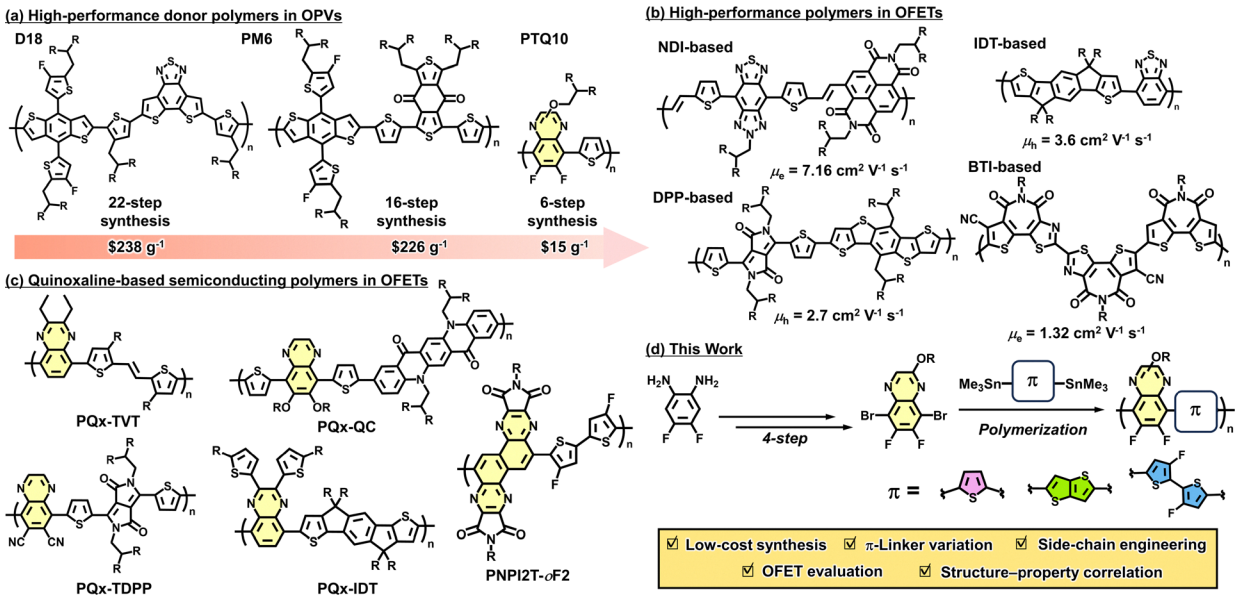

Fig. 1 Comparison of representative polymer semiconductors and the design concept of this work. (a) Representative high-performance donor polymers used in OPVs. (b) Representative high-performance polymer semiconductors for OFETs. (c) Previously reported quinoxaline-based semiconducting polymers for OFET applications. (d) This work: a cost-efficient quinoxaline-based polymer platform.

These problems hinder the practical implementation of semiconducting polymers.[28]

To overcome this challenge, the field of organic electronics has recently made rapid progress in polymer development—these polymers feature simple molecular structures that can be easily synthesized through straightforward reaction steps yet exhibit high performance.[29–32] A representative material, poly[[6,7-difluoro[(2-hexyldecyl)oxy]-5,8-quinoxalinediyl]-2,5-thiophenediyl] (PTQ10), features a quinoxaline core (Fig. 1a).[33–35] PTQ10 can be synthesized from conventional starting chemicals in just five reaction steps.[36] Moreover, functionalization of the quinoxaline moiety allows precise tuning of energy levels related to electron density and charge transport properties.[37] Consequently, quinoxaline-based polymers have attracted considerable interest as building blocks for low-cost, high-performance organic electronic materials.[38–40] Recent studies have also explored the application of quinoxaline-based donor polymers in OFETs. PTQ10-based polymers reported by Campoy-Quiles and co-workers exhibited a hole mobility of 2.45×10^{-3} cm^2 V^{-1} s^{-1}.[41] Guha and co-workers achieved comparable mobility by introducing thienylenevinylene (TVT) units into the quinoxaline backbone (Fig. 1c and Table S1).[42] However, systematic investigations of PTQ10-based polymers in OFETs remain limited,[43–47] as the relationships between the molecular structure, thin-film morphology, and device performance have not been fully elucidated.

In this study, we synthesized a series of quinoxaline-based polymers by systematically modifying their π-linker units and alkyl side-chain structures and comprehensively investigated their OFET performance. Density functional theory (DFT) calculations indicate that the synthesized polymers adopt highly planar conformations through noncovalent interactions, such as S–F and S–N interactions, conferring strong aggregation propensity, a property validated by spectroscopic techniques. Thin-film transistors based on these polymers exhibited competitive charge carrier mobilities relative to previously reported PTQ10-based polymers. Furthermore, grazing-incidence wide-angle X-ray scattering (GIWAXS) measurements reveal the correlation between molecular packing and charge transport properties (Fig. 1d).

2. Results and discussion

2.1. Synthesis

The synthetic routes and polymerization conditions for quinoxaline-based monomers are summarized in Scheme 1. Dibromoquinoxaline derivative **Qx-3** was synthesized from commercially available 1,2-diamino-4,5-difluorobenzene (**1**) *via* a previously reported procedure (Scheme 1a).[36] Notably, the intermediate was purified solely by precipitation without chromatographic purification, yielding a final overall yield of 71%. Monomer **Qx-4** was obtained by introducing a 2-hexyldecyl group onto **Qx-3** *via* a Mitsunobu reaction. Using the P(*tert*-Bu)$_3$ Pd G3 catalyst, **Qx-4** was polymerized with stannylated thiophene-based monomers *via* Stille coupling (Scheme 1b).[48] Detailed polymerization conditions employed in this study are summarized in Table S2. The polymerization of **P1**, containing a thiophene linker, proceeded homogeneously throughout. However, precipitation was observed during the polymerizations of **P2** and **P3**, which contain thieno[3,2-*b*]thiophene or fluorinated bithiophene linkers. This behavior is attributed to enhanced aggregation induced by the more planar donor units. After 24 h of polymerization, all polymers

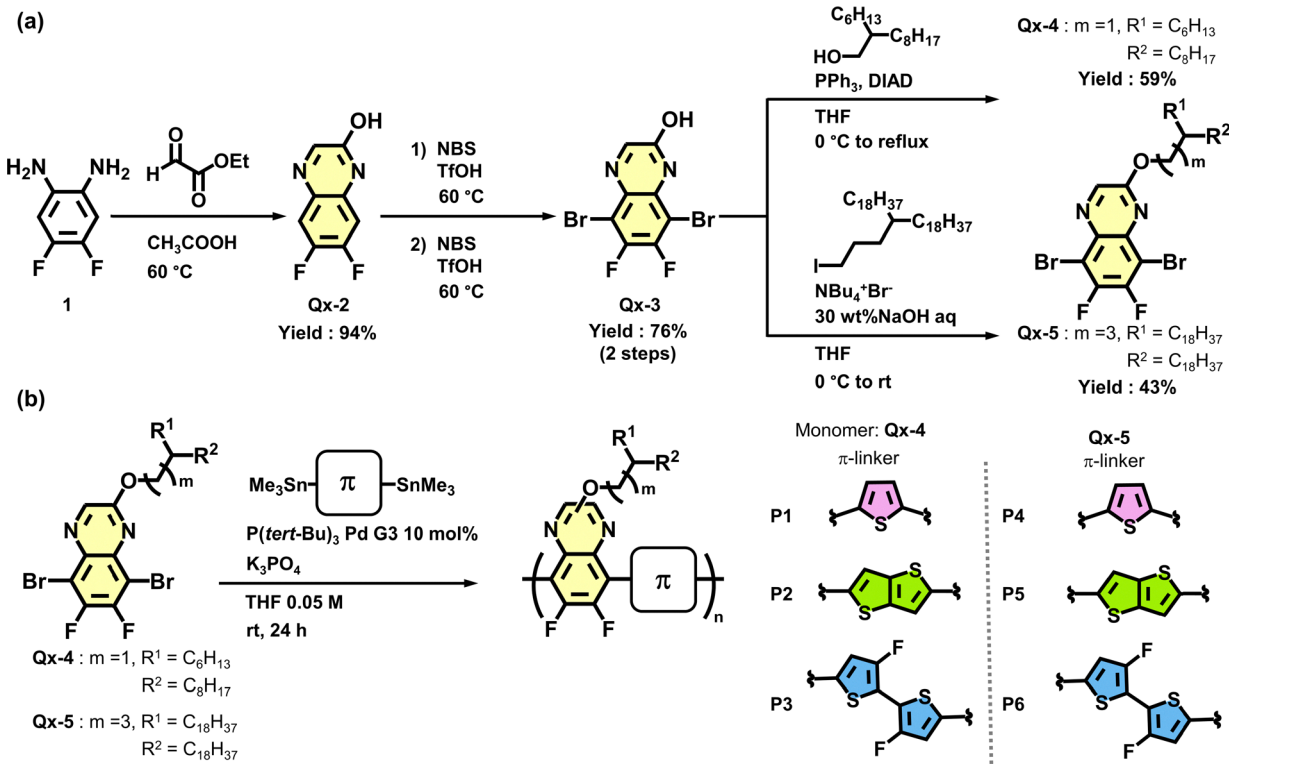

Scheme 1 (a) Synthesis of quinoxaline-based monomers **Qx-4** (short alkyl side chains) and **Qx-5** (long alkyl side chains). (b) Synthesis of quinoxaline-based conjugated polymers **P1–P6** *via* Stille polycondensation using different π-linkers.

were purified *via* Soxhlet extraction with methanol and acetone to remove catalyst residues, residual monomers, and low-molecular-weight fractions. For **P1**, the dichloromethane-extracted fraction was reprecipitated in methanol and collected by filtration. **P2** and **P3** were obtained by reprecipitating the chloroform fraction collected after dichloromethane extraction. Gel permeation chromatography (GPC) analysis revealed that the number-average molecular weight (M_n) of **P1** was determined to be 10.8 kg mol^{-1}, while the M_n values of the poorly soluble **P2** and **P3** were significantly reduced to 3.3 and 4.6 kg mol^{-1}, respectively (Table 1 and Fig. S1a). The reduced molecular weights of **P2** and **P3** likely stem from their strong aggregation tendency, causing precipitation before growth into high-molecular-weight products. Consistent with this finding, **P1** readily dissolves in common chlorinated solvents like chloroform and chlorobenzene at room temperature, whereas **P2** and **P3** require heating to form homogeneous solutions.

To obtain higher-molecular-weight polymers, polymer solubility must be enhanced to suppress precipitation. Therefore, monomer **Qx-5** bearing a longer alkyl chain was synthesized *via* the Williamson etherification reaction and polymerized under conditions similar to those for **Qx-4** (Scheme 1). Even with thieno[3,2-*b*]thiophene or fluorinated bithiophene linkers, the extended alkyl side chain suppressed precipitation, indicating significantly improved solubility of the resulting polymers. After reactions, crude products were purified by Soxhlet extraction (the same as that for **P1–P3**). **P4–P6** were obtained by reprecipitation of their hexane-extracted fractions in methanol. GPC analysis revealed that the M_n values of **P4–P6** all exceeded 11 kg mol^{-1}, substantially higher than those of the short-chain alkyl **Qx-4**-based polymers. These results suggest that the enhanced solubility facilitated the attainment of high molecular weights (Table 1 and Fig. S1b). Furthermore, **P4–P6** dissolve in chloroform and chlorobenzene without heating, implying high solution processability suitable for OFET fabrication.

The synthetic complexity of quinoxaline-based polymers was evaluated using the synthetic complexity index (SCI). The SCI quantitatively assesses the synthetic complexity of polymers relative to reported materials by integrating factors such as the number of reaction steps, overall yields, the number and type of purification processes, and hazardous chemical usage.[49,50] Using an SCI value of 100 for the commonly used organic

Table 1 Physicochemical properties and synthetic complexity of **P1–P6**

	M_n[a]/kg mol^{-1}	M_w[a]/kg mol^{-1}	PDI[ab]	Yield	SCI[c]	T_{5d}[d]/°C
P1	10.8	20.1	1.86	27%	31.7	367.5
P2	3.3	5.4	1.62	45%	27.1	315.8
P3	4.6	9.5	2.07	21%	32.2	369.0
P4	23.5	43.6	1.85	85%	25.6	364.2
P5	11.2	25.7	2.29	76%	26.3	351.5
P6	13.1	26.9	2.06	66%	27.3	370.9

[a] Determined by GPC using 1,2-dichlorobenzene as the eluent at 40 °C. [b] Polydispersity index (M_w/M_n). [c] Synthetic complexity index, a relative metric representing synthetic complexity, normalized to the D18 synthesis as the reference (0–100). [d] Temperature at the 5% weight loss, determined by TGA.

photovoltaic material donor D18 as a benchmark, the estimated SCI value for **P1** is 31.7.[16] This value indicates that the synthetic complexity of **P1** has been reduced to one-third that of D18 (Table 1 and Table S3). The reduced synthetic complexity of **P1** mainly originates from fewer reaction steps and simplified purification methods—in contrast to the D18 synthesis process, which requires 22 multistep reactions and column chromatography purification. In addition, the absence of hazardous reagents in the synthesis process significantly contributes to **P1**'s low SCI value. These results demonstrate that quinoxaline-based polymers are more suitable for large-scale production and can effectively reduce environmental impacts compared to previously reported semiconducting polymers. Notably, diketopyrrolopyrrole (DPP)-based polymers are widely used as key building blocks for high-performance OFETs,[7,22,23] and some derivatives, including fluorinated thiophene–DPP systems such as fDT-DPP, exhibit ambipolar charge transport.[51] However, these systems generally require more complex synthetic procedures, whereas the present polymers exhibit SCI values in the range of 40–50, highlighting their reduced synthetic complexity (Table S4).

To evaluate the thermal stability and phase transition behavior of **P1–P6**, thermogravimetric analysis (TGA) and differential scanning calorimetry (DSC) measurements were performed. The TGA curves showed that all polymers exhibited a 5% weight-loss temperature (T_{5d}) above 300 °C, indicating sufficient thermal stability to meet the requirements for OFET applications (Table 1 and Fig. S2). In DSC measurements, **P1–P3** bearing short alkyl chains showed no thermal transitions attributable to melting or crystallization during either heating or cooling scans within the temperature range. In contrast, **P4–P6**, due to their longer alkyl chains, exhibited endothermic peaks near 30 °C during heating and exothermic peaks during cooling, which are attributed to the melting and crystallization of the long alkyl chains (Fig. S3).[52]

2.2. Optical and electrochemical properties and theoretical calculations

To elucidate the influence of π-linkers on optical properties of the polymers, UV–vis absorption spectroscopy measurements were performed. Under chloroform dilution conditions, all polymers exhibited absorption bands in the 300–400 nm region (attributed to π–π* transitions) and broad absorption bands in the 400–700 nm region (attributed to intramolecular charge-transfer (ICT) transitions).[53] Upon heating these solutions, the absorption maxima (λ_{max}) showed a pronounced blue shift, accompanied by significant spectral shape changes (Fig. 2a and Fig. S4–S7). These observations indicate partial dispersion of the polymer aggregates formed at room temperature upon heating. Comparing the λ_{max} values of the dispersed polymers at 55 °C, those containing thiophene linkers (**P1** and **P4**) exhibited more blue-shifted λ_{max} values (*ca.* 505 nm) compared to the other polymers (Table 2). This result suggests that the photophysical properties are primarily governed by the effective conjugated length, which is related to the electron-donating character of the linker units and the backbone planarity. Upon cooling the heated solutions to 15 °C, the original spectra were recovered, demonstrating the thermo-reversibility of the polymer aggregation (Fig. S4–S7).[54]

To theoretically elucidate the differential effects of π-linkers on absorption and aggregation properties, trimer models were subjected to structural optimization and natural bond orbital (NBO) analysis using density functional theory (DFT, ωB97XD/6-31G(d,p) level). The optimized backbone structures are shown

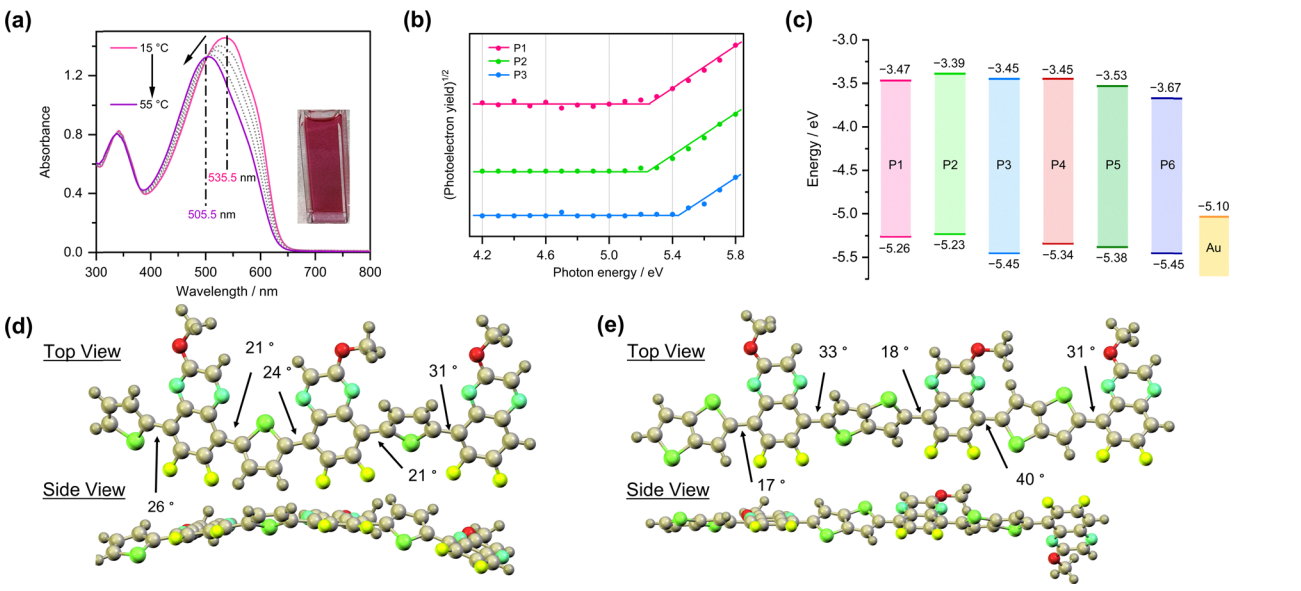

Fig. 2 (a) Temperature-dependent UV–vis absorption spectra of **P1** dissolved in chloroform solution (*c* = *ca.* 1.0 × 10^{-5} M) recorded from 15 to 55 °C. (b) PYS spectra of **P1–P3** in the thin-film state. (c) Energy level diagram of **P1–P6** in the thin-film state estimated from PYS measurements. The work function of Au is included for comparison. (d) and (e) Optimized geometries and conformational analysis of (d) **P1** and **P4** and (e) **P2** and **P5** models calculated at the ωB97XD/6-31G(d,p) level.

Table 2 Optical absorption and energy levels of polymers **P1–P6**

	λ_{max}^{sol} [a]/nm	λ_{max}^{film}/nm	E_{opt}^{gap} [b]/eV	E_{HOMO} [c]/eV	E_{LUMO} [d]/eV
P1	505.5	554, 597.5	1.79	−5.26	−3.47
P2	531	562, 609.5	1.84	−5.23	−3.39
P3	523.5	560, 616.5	1.83	−5.45	−3.45
P4	504	557.5, 607.5	1.89	−5.34	−3.45
P5	569	572, 622	1.85	−5.38	−3.53
P6	554.5	557.5, 607.5	1.78	−5.45	−3.67

[a] The maximum absorption wavelengths were determined from solution UV–vis spectra measured at 55 °C. [b] The optical band gaps (E_{opt}^{gap}) were estimated from the absorption onset of the thin film UV–vis spectra. [c] The HOMO energy levels (E_{HOMO}) were determined by PYS using thin films fabricated under the same conditions as the OFET devices. [d] Estimated as $E_{LUMO} = E_{HOMO} + E_{opt}^{gap}$.

in Fig. 2d and e and Fig. S8, with the corresponding molecular orbitals depicted in Fig. S9. Across all thiophene-based donor models, the dihedral angles between adjacent units ranged from 0 to 40°. Structural comparisons revealed that the thiophene-incorporated models exhibited twisted conformations, whereas the introduction of thieno[3,2-*b*]thiophene and fluorinated bithiophene resulted in more planar backbone structures. Both models confirm intramolecular S–N and S–F interactions with spatial penetration. The interatomic distances in the optimized structures were approximately 0.27–0.28 nm for S–N and 0.28–0.29 nm for S–F. These distances were shorter than the sum of the corresponding van der Waals radii, suggesting weak noncovalent interactions.[32] Unlike thiophene, the extended thieno[3,2-*b*]thiophene and fluorinated bithiophene units showed stronger S–N and S–F interactions. These interactions suppress conformational freedom around the bond axis, leading to a more planar and rigid backbone. Notably, the fluorinated bithiophene model showed the highest planarity due to the multipoint nature of these interactions. The NBO analysis further confirmed the orbital interactions corresponding to S–N and S–F bonds, corroborating the planarity of the backbone (Fig. S9).[32,55]

The energy levels of **P1–P6** were evaluated *via* photoelectron yield spectroscopy (PYS) and cyclic voltammetry (CV) (Table 2 and Fig. 2b and c, and Fig. S10). PYS measurements were conducted in air, with film preparation following the same procedures as that for OFET devices exhibiting the highest carrier mobilities (*vide infra*). Although all polymers exhibited similar HOMO energy levels within the range of −5.23 to −5.45 eV, **P3** and **P6** featured deeper HOMO levels than the other polymers due to the electron-withdrawing nature of fluorine atoms in their donor units. CV measurements revealed well-defined redox waves for all polymers. Their HOMO energy levels, referenced to the ferrocene/ferrocenium redox couple, show good agreement with PYS estimates (see Table 2 and Table S5 and Fig. S11). The LUMO energy levels estimated by combining optical band gaps and PYS-determined HOMO levels ranged from −3.39 to −3.67 eV, consistent with electrochemical measurements. These energy levels suggest that gold (Au) with a work function of −5.1 eV is suitable for both hole and electron injection in OFET devices based on **P1–P6**.[56,57]

2.3. Charge transport properties in OFET devices

The charge-transport properties of quinoxaline-based polymers were investigated by fabricating top-contact/bottom-gate (TC/BG) polymer thin-film transistors (Fig. S12). The organic semiconductor layers were formed by spin-casting polymer solutions (*c* = *ca.* 4–6 g L^{-1} in chloroform) onto SiO_2 (300 nm)/n^{++}–Si substrates modified with octadecyltrimethoxysilane (OTMS) self-assembled monolayers (SAMs) in a nitrogen-filled glovebox. After thermal annealing at temperatures ranging from 100 to 300 °C, gold source and drain electrodes were deposited *via* thermal evaporation. Detailed device fabrication procedures are provided in the Supplementary Information.[56] p-Type OFET characteristics were evaluated in air for all devices. For **P6**, both p- and n-type characteristics were also evaluated under vacuum conditions to ensure a reliable assessment of ambipolar transport. Current–voltage curves for devices fabricated based on **P1–P6** are shown in Fig. 3 and Fig. S13–S15, with extracted parameters summarized in Table 3.

P1–P5 exhibited unipolar p-type charge transport behavior, whereas **P6** demonstrated a balanced ambipolar behavior with a hole-to-electron mobility ratio (μ_h/μ_e) of 0.99, as measured under vacuum conditions for both p- and n-type operation. This behavior is likely associated with the fluorinated linker unit and superior film morphology of **P6** results in a lower electron injection barrier (Schottky barrier) between it and gold electrodes compared to that of other polymers, collectively enabling ambipolar charge transport.[58] It is generally expected that electron injection from gold electrodes is less favorable than hole injection due to the larger energetic offset between the electrode work function and the LUMO level compared to the HOMO level. However, transfer line method (TLM) analysis revealed that the contact resistance for hole transport was higher than that for electron transport ($R_{C,e}$ W = 3.24 × 10^7 Ω cm at V_G = −100 V and $R_{C,e}$ W = 5.18 × 10^6 Ω cm at V_G = +100 V, respectively; Fig. S16 and Table S6).[59] These results indicate that, although hole injection is energetically more favorable, electron transport may benefit from lower contact resistance, which could result in comparable charge carrier mobilities. Among all polymers, **P1** annealed at 300 °C exhibited the highest average hole mobility of 2.45 × 10^{-2} cm^2 V^{-1} s^{-1} (Fig. 3a). Compared to previously reported PTQ10-based polymers employing a quinoxaline scaffold, the hole mobility of **P1** is approximately one order of magnitude higher (Table S1). **P2** and **P3** exhibited hole mobilities approximately half that of **P1** (Fig. 3b and c). While increasing the annealing temperature enhanced the hole mobility for **P1–P3**, excessive annealing caused a decrease in mobility for **P4–P6**, which possess longer alkyl side chains. Notably, the charge transport properties of **P4** were completely impaired after 100 °C annealing (Fig. S17). This behavior arises from thermal activation of the long alkyl chains at elevated temperatures, which disrupts the molecular ordering within the film. Consequently, despite being the highest molecular weight polymer synthesized, **P4** exhibited a mobility two orders of magnitude lower than **P1**. Variations in molecular weight among **P1–P6** may influence the observed device performance, but the backbone

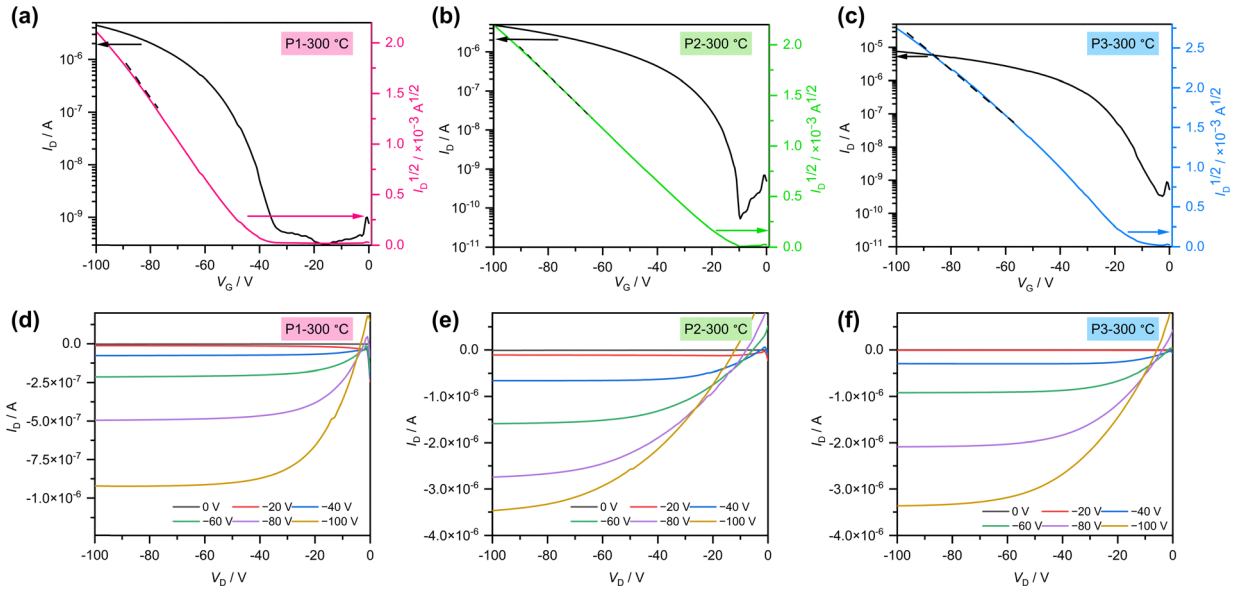

Fig. 3 Transfer characteristics (I_D–V_G) of OFET devices fabricated from (a) **P1**, (b) **P2**, and (c) **P3** thin films after thermal annealing at 300 °C, measured in air at a fixed drain voltage of V_D = −100 V. Output characteristics (I_D − V_D) of the corresponding devices are shown for (d) **P1**, (e) **P2**, and (f) **P3**, measured at gate voltages ranging from 0 to −100 V.

Table 3 Summary of OFET performance parameters, including charge carrier mobility (μ), threshold voltage (V_{th}), and current on/off ratio (I_{on}/I_{off}), for polymers **P1–P6** under optimized annealing conditions

Polymer	Annealing (°C)	Operation mode	Condition	μ (μ_{max})[a]/cm^2 V^{-1} s^{-1}	V_{th}/V	I_{on}/I_{off}[b]
P1	300	p-Type	In air	$(2.45 \pm 0.31) \times 10^{-2}$ (2.78×10^{-2})	−36.9 ± 4.1	10^3–10^4
P2	300	p-Type	In air	$(1.04 \pm 0.09) \times 10^{-2}$ (1.18×10^{-2})	−11.3 ± 3.6	10^2–10^5
P3	300	p-Type	In air	$(1.46 \pm 0.12) \times 10^{-2}$ (1.58×10^{-2})	−6.8 ± 7.2	10^4–10^6
P4	As cast	p-Type	In air	$(1.50 \pm 1.37) \times 10^{-4}$ (3.20×10^{-4})	−36.9 ± 14.7	10^2–10^4
P5	200	p-Type	In air	$(2.25 \pm 0.51) \times 10^{-3}$ (2.62×10^{-3})	−22.5 ± 8.3	10^0–10^1
P6	200	p-Type	In air	$(9.26 \pm 4.42) \times 10^{-4}$ (1.59×10^{-3})	−26.0 ± 14.7	10^1
	200	p-Type	Under vacuum	$(1.07 \pm 0.23) \times 10^{-3}$ (1.45×10^{-3})	−11.0 ± 6.2	10^1–10^2
	200	n-Type	Under vacuum	$(1.08 \pm 0.45) \times 10^{-3}$ (1.60×10^{-3})	−23.2 ± 21.7	10^1–10^2

[a] The values are presented as mean ± standard deviation (SD) obtained from five independent OFET devices, and the values in parentheses correspond to the highest mobility. [b] I_{on}/I_{off} ratios are reported as order-of-magnitude ranges estimated from the transfer characteristics.

structure appears to be the primary determining factor.[18,60] For instance, the hole mobility of **P4** was much lower than those of **P5** and **P6**, which employed thieno[3,2-*b*]thiophene and fluorinated bithiophene linkers, respectively. This result suggests that enhanced backbone planarity in **P5** and **P6** is likely to promote aggregation, which may contribute to improved molecular ordering in the thin films, consistent with the absorption spectroscopy and DFT results.

2.4 Film morphology

To elucidate the relationship between the chemical structures of **P1–P6** and their carrier mobilities, we systematically investigated the thin-film morphology and polymer orientation using UV–vis absorption spectroscopy, GIWAXS, and atomic force microscopy (AFM). UV–vis absorption spectra of the polymer films revealed bathochromic shifts in the absorption maxima for all polymers compared to their partially dispersed state in chloroform (Fig. S18). In addition, the thin-film spectra revealed a significant increase in the absorption intensities of the 0–0 vibronic peaks. This spectral trend resembles phenomena observed during the cooling of dilute solutions. After annealing treatment, the absorption intensities of the 0–0 vibronic peaks slightly increased, indicating a rearrangement of polymer chains.

The surface morphology of the films was examined using AFM. For films of **P1** and **P4** incorporating thiophene π-linkers, the AFM images exhibited relatively uniform granular morphology (Fig. S19 and Fig. S20). After annealing at 300 °C, structural enlargement was observed, while the root-mean-square (RMS) roughness of **P1** increased from 2.81 to 10.7 nm (Fig. 4a and Fig. S19). Notably, the annealed **P4** showed surface morphology disruption, inhibiting chain rearrangement, which is consistent with restricted chain mobility at elevated temperatures (Fig. S20). To further understand the thermal instability of **P4**, AFM measurements were performed after thermal annealing at 100 °C and 200 °C (Fig. S21). With increasing annealing temperature, the long alkyl side chains became more mobile, leading to local aggregation and morphological disorder.

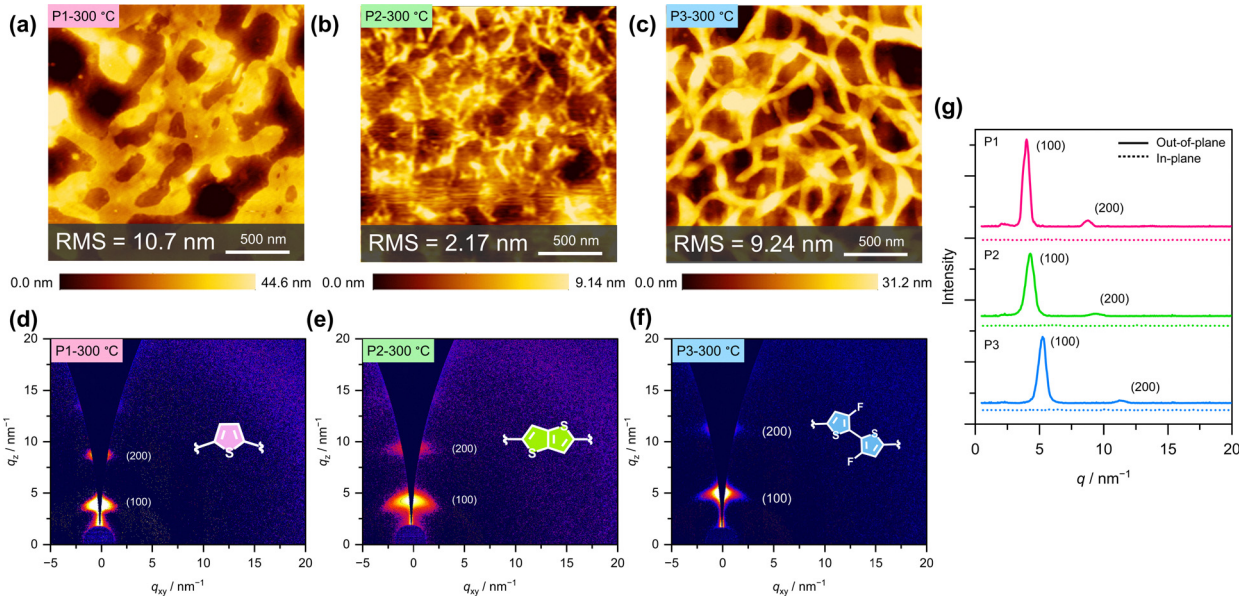

Fig. 4 AFM height images of polymer thin films annealed at 300 °C: (a) **P1**, (b) **P2**, and (c) **P3**. The RMS roughness values are indicated in each panel (scan size: 2 × 2 μm^2). GIWAXS patterns of the corresponding thin films after annealing at 300 °C: (d) **P1**, (e) **P2**, and (f) **P3**. (g) One-dimensional line cuts extracted from the GIWAXS patterns along the out-of-plane (solid lines) and in-plane (dotted lines) directions, highlighting the (100) lamellar stacking and the higher-order (200) diffraction peaks.

Such structural changes are likely to disrupt charge percolation pathways, which explains the complete loss of OFET performance after annealing. Other polymers possessing highly planar backbone conformations formed nanofibrillar structures immediately after spin-coating.[61] The morphological differences between **P1** and **P4** suggest that introducing thieno[3,2-*b*]thiophene or fluorinated bithiophene units enhances interchain interactions. Thermal annealing promotes structural transformation from short, fine fibrous structures to larger aggregates through polymer chain rearrangement (Fig. 4b and c and Fig. S19 and S20).

To investigate the polymer stacking structure in the thin films, films were prepared on Si substrates using the same procedures as device fabrication and subjected to GIWAXS measurements. The resulting two-dimensional diffraction images and one-dimensional patterns in the out-of-plane and in-plane directions are shown in Fig. 4d–g and Fig. S22. Structural parameters extracted from the out-of-plane lamellar diffraction peaks, including q_z, interlayer distance (d_{lamellar}), full width at half maximum (FWHM), and crystal coherence length (CCL), are summarized in Table 4 and Table S7. After annealing, all polymers exhibited diffraction peaks attributable to lamellar (h00) orientation exclusively in the out-of-plane direction. This diffraction pattern exhibits the characteristic of edge-on orientation, which may be beneficial for charge transport in OFETs.[62] Notably, when **P1** is used as a p-type material in OPV devices, it has been reported in the literature to adopt a face-on orientation.[54,63] This likely stems from the differing deposition conditions between OPVs and OFETs. In OPV fabrication, **P1** was co-deposited with acceptor materials onto a hydrophilic PEDOT:PSS layer, rather than onto hydrophobic SAM-modified Si substrates employed in the present OFET devices. The full width at half maximum (FWHM) of the diffraction peaks for **P2** was larger than that for **P1**, indicating lower crystallinity. This reduced crystallinity may be related to lower hole mobility of **P2** compared to that of **P1**. Although **P1**–**P3** displayed (100) and (200) crystal planes originating from lamellar ordering, **P4** with long alkyl side chains exhibited diffraction peaks extending to the (300) crystal plane (Fig. 4 and Fig. S22). By employing thieno[3,2-*b*]thiophene and fluorinated bithiophene linkers, **P5** and **P6** exhibited diffraction peaks attributable to (400) and (500) crystal planes, respectively (Fig. S22). These results suggest that the elongation of the alkyl side chains enhances van der Waals interactions through interdigitated arrangements between alkyl chains, leading to the formation of lamellar structures with longer-range order. The higher-order lamellar diffraction peaks of **P5** and **P6** were more distinct than those of **P4**, indicating improved lamellar ordering in the films. This enhanced ordering may contribute, together with other factors such as backbone planarity and

Table 4 Out-of-plane (100) lamellar packing parameters of polymers **P1**–**P6** evaluated by GIWAXS

		Out-of-plane (100)			
	Annealing (°C)	q_z/nm^{-1}	d_{lamellar}/nm	FWHM/nm^{-1}	CCL/nm
P1	300	3.98	1.58	0.679	8.33
P2	300	4.27	1.47	0.743	7.61
P3	300	5.23	1.20	0.679	8.33
P4	As cast	2.09	3.01	0.297	19.0
P5	200	2.09	3.00	0.287	19.7
P6	200	2.28	2.75	0.534	10.6

molecular ordering, to the higher hole mobilities observed for **P5** and **P6** compared to that of **P4**. Although the charge carrier mobility of **P4–P6** is relatively low in the present study, their relatively high crystallinity suggests that the molecular design is fundamentally appropriate for efficient charge transport. The limited performance is therefore more likely attributed to insufficient film morphology optimization rather than intrinsic material limitations. Further optimization of processing conditions is expected to unlock their full potential.

Notably, although UV–vis absorption measurements indicate aggregation in quinoxaline-based polymer films, no distinct diffraction peaks originating from the (010) crystal plane (corresponding to π–π stacking) were observed for any polymer. This may result from the random regioregularity due to the asymmetric structure of the quinoxaline monomer. As the alkyl side chains are randomly oriented, the polymer backbone may undergo distortion due to steric hindrance. The asymmetric structure and reduced planarity may collectively impede the formation of uniform π–π stacking.[64]

Finally, device stability was evaluated *via* storage in a nitrogen-filled glovebox (Fig. S23). These measurements correspond to the storage stability of the devices under an inert atmosphere. Time-dependent measurements of hole mobility revealed that the performance of **P1** decreased to 48% of its initial value after 21 days; that of **P2** and **P3** decreased to *ca.* 20% and 5%, respectively, within 15 days. In contrast, **P4–P6** with longer alkyl side chains maintained hole mobility exceeding 70% of their initial values after 17 days. This enhanced stability is likely associated with the increased molecular weight, improved crystallinity, and greater hydrophobicity—properties that effectively mitigate device deterioration caused by moisture and oxygen permeation.[65,66] Furthermore, to evaluate operational stability, transfer characteristics of **P1**, which exhibited the highest mobility in this study, were measured over 50 consecutive cycles in air (Fig. S24). No noticeable differences were observed between the 1–25 and 26–50 cycles, suggesting stable device operation under the tested conditions.[19]

3. Conclusions

In this study, we successfully synthesized a series of semiconducting polymers based on a quinoxaline core through a simple and low-cost synthesis procedure. By systematically varying the π-linker units and alkyl side-chain lengths, quinoxaline-based polymers **P1–P6** were synthesized, and their OFET performances and thin-film structures were comprehensively evaluated. Within this series, **P1** exhibited the highest average hole mobility of 2.45×10^{-2} $cm^2 V^{-1} s^{-1}$, representing an improvement over PTQ10-based OFETs. Extending the π-linker enhances backbone planarity and promotes aggregation through intramolecular noncovalent interactions, yet yields lower hole mobilities than **P1**. Conversely, combining a fluorinated bithiophene π-linker with a longer alkyl chain achieved balanced ambipolar charge transport properties. GIWAXS revealed that despite variations in π-linker units and alkyl chain lengths, all polymers formed edge-on orientations, conducive to efficient charge transport in OFETs. In polymers bearing long alkyl side chains, replacing the thiophene linker with thieno[3,2-*b*]thiophene or fluorinated bithiophene enhanced backbone planarity and strengthened intermolecular interactions. These results demonstrate that π-linker engineering effectively modulates backbone planarity, intermolecular interactions, and thin-film crystallinity, which may influence charge transport properties. Furthermore, the synergistic effects of the fluorinated comonomer and long alkyl side chains enabled polymer thin films to form structures conducive to electron transport, thereby achieving ambipolar charge transport in **P6**. Combining π-linker optimization with control over molecular orientation through side-chain regioregularity holds promise for further enhancing charge transport properties.[67–69] Overall, this study provides insights into rational molecular design principles for developing quinoxaline-based semiconducting polymers with low synthetic complexity and scalable material frameworks, providing practical guidelines for next-generation organic field-effect transistors.

Author contributions

Y. O. performed all experimental work, including the synthesis of all polymers, device fabrication and performance evaluation, calculations, and data analysis (including GIWAXS), as well as validation, visualization, writing – original draft, and writing – review and editing. A. I. contributed to methodology development, data analysis, validation, supervision, funding acquisition, writing – original draft, and writing – review and editing. T.-Y. W. performed the GIWAXS measurements. C.-C. C. supervised the GIWAXS measurements and contributed to validation and writing – review and editing. M. W. provided technical advice, contributed to validation, and engaged in fruitful discussions regarding the polymerization. T. M. contributed to conceptualization, funding acquisition, methodology, project administration, supervision, and writing – review and editing. All authors have given approval to the final version of the manuscript.

Conflicts of interest

The authors have no conflicts of interest.

Data availability

The data that support the findings of this study are available from the corresponding author upon reasonable request.

Supplementary information (SI) is available. See DOI: https://doi.org/10.1039/d6tc00601a.

Acknowledgements

This study was partly supported by Japan Society for the Promotion of Science (JSPS) KAKENHI grant numbers JP24H0005

(T. M.) and JP24K23077 (A. I.). Computational calculations were carried out using the TSUBAME4.0 supercomputer at the Institute of Science Tokyo, particularly for DFT calculations. The authors also acknowledge the National Synchrotron Radiation Research Center (NSRRC) of Taiwan for the GIWAXS experiments in BL23A1 (TLS).

References

1 X. Wu, W. Fu and H. Chen, *ACS Appl. Polym. Mater.*, 2022, **4**, 4609–4623.
2 X. Xu, Y. Zhao and Y. Liu, *Small*, 2023, **19**, 202206309.
3 X. Wan, C. Li, M. Zhang and Y. Chen, *Chem. Soc. Rev.*, 2020, **49**, 2828–2842.
4 J. Yi, G. Zhang, H. Yu and H. Yan, *Nat. Rev. Mater.*, 2024, **9**, 46–62.
5 H. Chen, W. Zhang, M. Li, G. He and X. Guo, *Chem. Rev.*, 2020, **120**, 2879–2949.
6 Y. Wang and T. Michinobu, *J. Mater. Chem. C*, 2016, **4**, 6200–6214.
7 Y. Wang and T. Michinobu, *J. Mater. Chem. C*, 2018, **6**, 10390–10410.
8 X. Liu, C. L. Anderson and Y. Liu, *Acc. Chem. Res.*, 2023, **56**, 1669–1682.
9 C. Wang, X. Zhang, H. Dong, X. Chen and W. Hu, *Adv. Energy Mater.*, 2020, **10**, 2000955.
10 S. Shoaee, H. M. Luong, J. Song, Y. Zou, T. Q. Nguyen and D. Neher, *Adv. Mater.*, 2024, **36**, 2302005.
11 L. Luo, W. Huang, C. Yang, J. Zhang and Q. Zhang, *Front. Phys.*, 2021, **16**, 33500.
12 J. Lee, *Asian J. Org. Chem.*, 2023, **12**, e202300104.
13 K. C. Chong, T. L. D. Tam, R. Tao, K. L. O. Chin, M. H. Chua and J. Xu, *Energy Mater. Adv.*, 2025, **6**, 0134.
14 A. Insuasty, S. Maniam and S. J. Langford, *Chem. – Eur. J.*, 2019, **25**, 7058–7073.
15 H. Jiang, S. Zhu, Z. Cui, Z. Li, Y. Liang, J. Zhu, P. Hu, H. L. Zhang and W. Hu, *Chem. Soc. Rev.*, 2022, **51**, 3071–3122.
16 J. J. Rech, J. Neu, Y. Qin, S. Samson, J. Shanahan, R. F. Josey, H. Ade and W. You, *ChemSusChem*, 2021, **14**, 3561–3568.
17 M. Liao, J. Duan, P. Peng, J. Zhang and M. Zhou, *RSC Adv.*, 2020, **10**, 41764–41779.
18 Y. Wang, T. Hasegawa, H. Matsumoto, T. Mori and T. Michinobu, *Adv. Mater.*, 2018, **30**, 1707164.
19 Y. Wang, T. Hasegawa, H. Matsumoto and T. Michinobu, *J. Am. Chem. Soc.*, 2019, **141**, 3566–3575.
20 A. Wadsworth, H. Chen, K. J. Thorley, C. Cendra, M. Nikolka, H. Bristow, M. Moser, A. Salleo, T. D. Anthopoulos, H. Sirringhaus and I. McCulloch, *J. Am. Chem. Soc.*, 2020, **142**, 652–664.
21 X. Zhang, H. Bronstein, A. J. Kronemeijer, J. Smith, Y. Kim, R. J. Kline, L. J. Richter, T. D. Anthopoulos, H. Sirringhaus, K. Song, M. Heeney, W. Zhang, I. McCulloch and D. M. DeLongchamp, *Nat. Commun.*, 2013, **4**, 2238.
22 H. J. Cheon, T. K. An and Y. H. Kim, *Macromol. Res.*, 2022, **30**, 71–84.
23 S. Park, B. T. Lim, B. Kim, H. J. Son and D. S. Chung, *Sci. Rep.*, 2014, **4**, 5482.
24 Y. Li, S. Gámez-Valenzuela, W. Yang, R. Ding, Y. Wei, E. Huang, X. Guo and K. Feng, *Macromolecules*, 2025, **58**, 7593–7604.
25 M. Ferrara, F. Della Negra and M. Verzini, *Org. Process Res. Dev.*, 2025, **29**, 1110–1124.
26 W. Liu, H. Shang, X. Xu and Z. Bo, *ACS Appl. Eng. Mater.*, 2025, **3**, 1102–1129.
27 M. Wakioka, *Polym. J.*, 2026, **58**, 103–116.
28 Y. H. Shih, G. L. Wu, P. H. Chueh, J. C. Chen, C. Y. Tsai, T. Y. Wang, M. H. Yu, Y. P. Li, W. C. Chen and C. C. Chueh, *JACS Au*, 2025, **5**, 1382–1391.
29 N. Yang, Y. Cui, Y. Xiao, Z. Chen, T. Zhang, Y. Yu, J. Ren, W. Wang, L. Ma and J. Hou, *Angew. Chem., Int. Ed.*, 2024, **63**, e202403753.
30 K. Yamanaka, T. Mikie and I. Osaka, *Adv. Energy Mater.*, 2025, **15**, 2502173.
31 K. Yamada, W. Suzuki, M. Kubota, J. Inamoto, M. Kondo, T. Koganezawa, Y. Chiga, R. Takahata, T. Teranishi, H. Imahori and T. Umeyama, *J. Mater. Chem. C*, 2025, **13**, 7984–7995.
32 Z. Li, R. Ding, X. Gu, C. Zhang, J. Lv, Y. Han, J. Chen, Y. Cai, X. Zhang and H. Huang, *Chem. Commun.*, 2025, **61**, 8659–8662.
33 C. Sun, F. Pan, H. Bin, J. Zhang, L. Xue, B. Qiu, Z. Wei, Z. G. Zhang and Y. Li, *Nat. Commun.*, 2018, **9**, 743.
34 C. Sun, S. Qin, R. Wang, S. Chen, F. Pan, B. Qiu, Z. Shang, L. Meng, C. Zhang, M. Xiao, C. Yang and Y. Li, *J. Am. Chem. Soc.*, 2020, **142**, 1465–1474.
35 A. L. Jones, C. H. Y. Ho, S. A. Schneider, J. Zhang, Y. Pei, J. Wang, X. Zhan, S. R. Marder, M. F. Toney, F. So, G. N. M. Reddy and J. R. Reynolds, *Chem. Mater.*, 2022, **34**, 6853–6867.
36 J. Kang, S. Y. Kim, H. H. Jo and K. Zong, *ChemSusChem*, 2024, **17**, e202400216.
37 Z. Abid, L. Ali, S. Gulzar, F. Wahad, R. S. Ashraf and C. B. Nielsen, *Beilstein J. Org. Chem.*, 2023, **19**, 1694–1712.
38 D. Gedefaw, M. Prosa, M. Bolognesi, M. Seri and M. R. Andersson, *Adv. Energy Mater.*, 2017, **7**, 1700575.
39 J. Yuan, J. Ouyang, V. Cimrová, M. Leclerc, A. Najari and Y. Zou, *J. Mater. Chem. C*, 2017, **5**, 1858–1879.
40 P.-Y. Gu, Z. Wang, G. Liu, H. Yao, Z. Wang, Y. Li, J. Zhu, S. Li and Q. Zhang, *Chem. Mater.*, 2017, **29**, 4172–4175.
41 S. Riera-Galindo, M. Sanz-Lleó, E. Gutiérrez-Fernández, N. Ramos, M. Mas-Torrent, J. Martín, L. López-Mir and M. Campoy-Quiles, *Small*, 2024, **20**, 2311735.
42 J. Barron, S. Attar, A. Ghobadi, S. Gangopadhyay, D. Sredojevic, M. Al-Hashimi and S. Guha, *ACS Appl. Electron. Mater.*, 2024, **6**, 1464–1474.
43 S. Gámez-Valenzuela, S. Ma, Y. Wei, Y. Lu, C. Xu, K. Feng, S. Y. Jeong, H. Wang, H. Y. Woo, A. Facchetti and X. Guo, *J. Am. Chem. Soc.*, 2025, **147**, 38851–38864.
44 H. Jung, K. Nakano and K. Tajima, *ACS Appl. Mater. Interfaces*, 2025, **17**, 66980–66987.
45 T. Mikie, K. Okamoto, Y. Iwasaki, T. Koganezawa, M. Sumiya, T. Okamoto and I. Osaka, *Chem. Mater.*, 2022, **34**, 2717–2729.

46 Z. Dai, D. Zhang and H. Zhang, *Front. Chem.*, 2022, **10**, 934203.
47 J. Jeon, H. Jhon, M. Kang, H. J. Song and T. K. An, *Org. Electron.*, 2018, **56**, 1–4.
48 B. Ma, Q. Shi, X. Ma, Y. Li, H. Chen, K. Wen, R. Zhao, F. Zhang, Y. Lin, Z. Wang and H. Huang, *Angew. Chem., Int. Ed.*, 2022, **61**, e202115969.
49 J. Kimpel, Y. Kim, H. Schomaker, D. R. Hinojosa, J. Asatryan, J. Martín, R. Kroon, M. Sommer and C. Müller, *Sci. Adv.*, 2025, **11**, eadv8168.
50 R. Po, G. Bianchi, C. Carbonera and A. Pellegrino, *Macromolecules*, 2015, **48**, 453–461.
51 M. Mamone, T. Bura, S. Brassard, E. Soligo, K. He, Y. Li and M. Leclerc, *Mater. Chem. Front.*, 2020, **4**, 2040–2046.
52 T. Lei, J. H. Dou, X. Y. Cao, J. Y. Wang and J. Pei, *Adv. Mater.*, 2013, **25**, 6589–6593.
53 P. C. Rodrigues, L. S. Berlim, D. Azevedo, N. C. Saavedra, P. N. Prasad, W. H. Schreiner, T. D. Z. Atvars and L. Akcelrud, *J. Phys. Chem. A*, 2012, **116**, 3681–3690.
54 D. Yuan, G. Qin, L. Zhang, F. Pan, R. Qiu, S. Lei and J. Chen, *ACS Appl. Mater. Interfaces*, 2021, **13**, 57654–57663.
55 C. Yorur Goreci, M. Kazici, S. Bozar, H. Gokce and S. Gunes, *J. Mater. Sci.: Mater. Electron.*, 2021, **32**, 14749–14763.
56 W. He, Q. Liu, S. Otep, H. Matsumoto, S. Manzhos, P. Sonar, A. K. K. Kyaw and T. Michinobu, *Chin. J. Chem.*, 2023, **41**, 1028–1036.
57 Q. Liu, S. Kumagai, S. Manzhos, Y. Chen, I. Angunawela, M. M. Nahid, K. Feron, S. E. Bottle, J. Bell, H. Ade, J. Takeya and P. Sonar, *Adv. Funct. Mater.*, 2020, **30**, 2000489.
58 M. Waldrip, O. D. Jurchescu, D. J. Gundlach and E. G. Bittle, *Adv. Funct. Mater.*, 2020, **30**, 1904576.
59 K. Shibata, H. Wada, K. Ishikawa, H. Takezoe and T. Mori, *Appl. Phys. Lett.*, 2007, **90**, 193509.
60 D. K. Tran, A. Robitaille, I. J. Hai, C.-C. Lin, D. Kuzuhara, T. Koganezawa, Y.-C. Chiu, M. Leclerc and S. A. Jenekhe, *Chem. Mater.*, 2022, **34**, 9644–9655.
61 N. E. Persson, P. H. Chu, M. McBride, M. Grover and E. Reichmanis, *Acc. Chem. Res.*, 2017, **50**, 932–942.
62 J. Rivnay, S. C. B. Mannsfeld, C. E. Miller, A. Salleo and M. F. Toney, *Chem. Rev.*, 2012, **112**, 5488–5519.
63 J. H. Kim, C. E. Song, W. S. Shin, B. Kim, I. N. Kang and D. H. Hwang, *J. Polym. Sci., Part A: Polym. Chem.*, 2015, **53**, 1904–1914.
64 R. Noriega, J. Rivnay, K. Vandewal, F. P. V. Koch, N. Stingelin, P. Smith, M. F. Toney and A. Salleo, *Nat. Mater.*, 2013, **12**, 1038–1044.
65 C. G. Tang, K. Hou and W. L. Leong, *Chem. Mater.*, 2024, **36**, 28–53.
66 J. Choi, M. J. Kim, J. Y. Kim, E. K. Lee, C. Lee, Y. Park, J. Kang, J. Il Park, B. J. Cho and S. G. Im, *Small Methods*, 2023, **7**, 2300628.
67 S. Guchait, L. Herrmann, K. Kadri, N. Leclerc, F. Tran Van and M. Brinkmann, *ACS Appl. Polym. Mater.*, 2023, **5**, 5676–5686.
68 Y. Kim, H. Park, J. S. Park, J. W. Lee, F. S. Kim and B. J. Kim, *J. Mater. Chem. A*, 2022, **10**, 2672–2696.
69 Y. Otake and T. Amaya, *Synth. Met.*, 2025, **314**, 117922.